Journal of Astronomical Telescopes, Instruments, and Systems

AstronomicalTelescopes.SPIEDigitalLibrary.org

Analytic approach for segment-level wavefront sensing in the global alignment progress based on image feature analysis

Guohao Ju
Boqian Xu
Di Zhang
Hongcai Ma
Xiaoquan Bai

SPIE.

Guohao Ju, Boqian Xu, Di Zhang, Hongcai Ma, Xiaoquan Bai, "Analytic approach for segment-level wavefront sensing in the global alignment progress based on image feature analysis," *J. Astron. Telesc. Instrum. Syst.* **6**(2), 029003 (2020), doi: 10.1117/1.JATIS.6.2.029003

Analytic approach for segment-level wavefront sensing in the global alignment progress based on image feature analysis

Guohao Ju,* Boqian Xu, Di Zhang, Hongcai Ma, and Xiaoquan Bai
Chinese Academy of Science, Changchun Institute of Optics, Fine Mechanics and Physics, Changchun, China

Abstract. Segmented mirror space telescopes have many advantages in both observation capacity and engineering feasibility. However, the alignment procedures for them are particularly complicated. Meanwhile, global alignment is one of the most important steps, in which the misalignments of each segment should be determined and corrected before image stacking is performed. Therefore, segment-level wavefront sensing is needed in this process. At present, traditional iterative phase retrieval algorithm is used to recover the segmented-level wavefront phase. However, the efficiency of this algorithm is comparatively low, especially given that there is an array of segment-level wavefront maps that need to be recovered. In addition, the magnitudes of misalignments are comparatively large in this stage and the iterative phase retrieval algorithm can be trapped in a local minimum for large-scale wavefront sensing. An analytic approach is proposed to estimate the segment-level wavefront aberrations based on the analysis of the geometrical features of one defocused point spread function (PSF) image. Meanwhile, some aberration properties of the misaligned system are also utilized. Simulations and an experiment are performed to verify the effectiveness of the proposed approach. This work can not only improve the efficiency and robustness of the global alignment of segmented mirror space telescopes, but also provide an intuitive and in-depth understanding for the mechanism of aberration calculation using PSF image features. [DOI: 10.1117/1.JATIS.6.2.029003]

Keywords: wavefront sensing; segmented mirror space telescopes; global alignment; geometrical feature of point spread function; aberration properties.

Paper 19123 received Dec. 10, 2019; accepted for publication Apr. 8, 2020; published online May 1, 2020.

1 Introduction

In order to observe a more distant and fainter object with a better resolution, space astronomical telescopes with a larger primary mirror (PM) are needed to improve the diffraction limit and increase the collected light energy. However, this will lead to problems with monolithic PM manufacture and testing, transportation and launch. Segmented PMs represent an efficient solution to these issues. At present, James Webb Space Telescope (JWST), which is a 6-m-class infrared space telescope, adopts a segmented PM, and it will be located in an orbit near the second Lagrange point (L2) to study and answer some fundamental astrophysical questions.[1,2]

Although the segmented configuration of the PM makes it feasible for the construction of extra-large space telescopes, it also poses great challenges for the active optical alignment of this class of telescopes after launch and initial deployment in orbit. Active optical alignment of segmented mirror space telescopes is also named "wavefront sensing and control (WFS&C)."[3–5] WFS&C process for JWST is shown in Fig. 1,[3] which includes a series of commissioning steps. At each given step, the dominant error is always the main emphasis. The wavefront error is decreased consistently step by step and the alignment of the system is improved gradually. WFS&C activities begin after the telescope is deployed and cooled to its operating temperature.

*Address all correspondence to Guohao Ju, E-mail: juguohao@ciomp.ac.cn

2329-4124/2020/$28.00 © 2020 SPIE

Global alignment is one of the most complicated and important steps in the active optical alignment procedures.[6] In this step, the 7 degrees of freedom (DOFs) of each PM segment and 6 DOFs of the secondary mirror (SM) need to be adjusted to eliminate the segment-level wavefront errors before image stacking. Therefore, segment-level wavefront sensing should be performed to determine the misalignment state of the system. At present, phase retrieval algorithm is used to recover the segment-level wavefront phase in the global alignment process.[5] This type of algorithm was originally developed to sense the wavefront for the Hubble Space Telescope.[7,8] It is based on the work of Gerchberg and Saxton[9,10] and model-based optimization.[11,12] In general, these algorithms require many iterations and are slow to converge. In the case of JWST, this is not a main concern since the computation time represents a small fraction of the total time spent aligning the telescope, which only needs to be aligned once. However, one could certainly imagine a situation where the computation time could be problematic (e.g., telescopes with many more segments or systems that required frequent realignment). In addition, the system is seriously misaligned, and the magnitudes of the segment-level aberrations are comparatively large after initial assembly or deployment of the segmented space telescope while iterative phase retrieval algorithms can be trapped in local minimum, especially for large-scale wavefront sensing.

To improve the efficiency and robustness of the global alignment process, we propose an analytic and noniterative approach to estimate the segment-level wavefront aberrations. On one hand, the magnitude of misalignments is usually very large in global alignment, and in this case the shape of the point spread function (PSF) can be described with geometrical optics (more specifically, the transverse aberrations of the marginal ray at the image plane). On the other hand, global alignment is performed before image stacking. In this process, a telescope with a segmented PM can be seen as an array of off-axis telescopes (each off-axis segment of the PM and the SMs compose an off-axis telescope). Off-axis telescopes have special aberration properties in misaligned state,[13–16] which can be utilized to estimate the wavefront aberrations. On this basis, we establish the analytic relations between Fringe Zernike aberration coefficients (C_4 to C_8) and several geometric features of the elliptical PSF (including the lengths of the major and minor axis and the azimuthal angle of the major axis) when certain magnitude of positive defocus aberration is introduced to the system. On this basis, we can noniteratively estimate the wavefront aberration coefficients with one defocused PSF.

The remainder of this paper is organized as follows. In Sec. 2, we give a brief review of the inherent relations between the astigmatism and coma in misaligned off-axis astronomical telescopes. Then in Sec. 3, we continue to propose an analytic and noniterative aberration estimation approach based on the analysis of the PSF image features and the understanding of aberration properties. In Secs. 4 and 5, we present detailed simulations as well as a real experiment to demonstrate the accuracy and practical feasibility of the proposed method, respectively. We summarize and conclude this paper in Sec. 6.

2 Review of the Inherent Relations Between the Astigmatism and Coma in Misaligned Pupil-Offset Off-Axis Telescopes

As shown in Fig. 1, global alignment process is implemented before image stacking. In this process, each off-axis segment and the SMs compose an off-axis telescope, and therefore, segment-level wavefront sensing can be seen as wavefront sensing for a series of misaligned off-axis telescopes. (The magnitudes of misalignments are usually very large in the global alignment process.) In this section, we will review some aberration properties of misaligned off-axis telescopes, which will serve as an important priori condition for the aberration estimation process (Fig. 2).

In misaligned pupil-offset off-axis astronomical telescopes, there exist three kinds of misalignments, i.e., lateral misalignments (decenter and tip-tilt of optical surfaces in the lateral direction), axial misalignments (dislocation of optical surfaces along the axial direction), and rotational misalignments (rotation of the surface with reference to their geometric center). We have discussed the aberration field characteristics induced by these three kinds of misalignments by extending nodal aberration theory[17–22] to pupil-offset off-axis systems.[13–16]

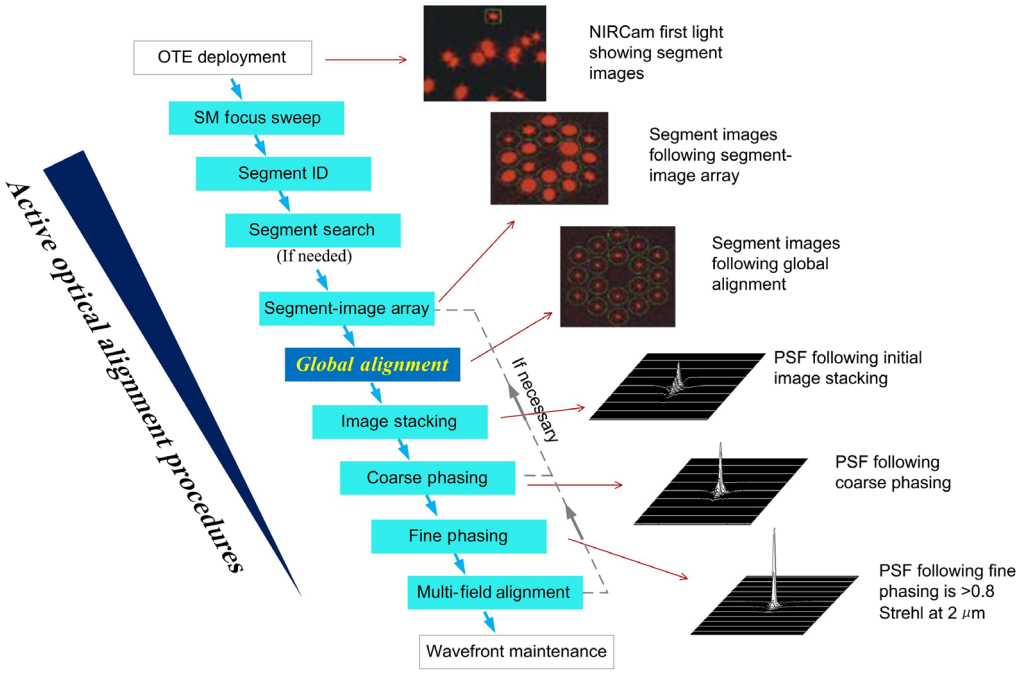

Fig. 1 Active optical alignment procedures for segmented mirror space telescopes.

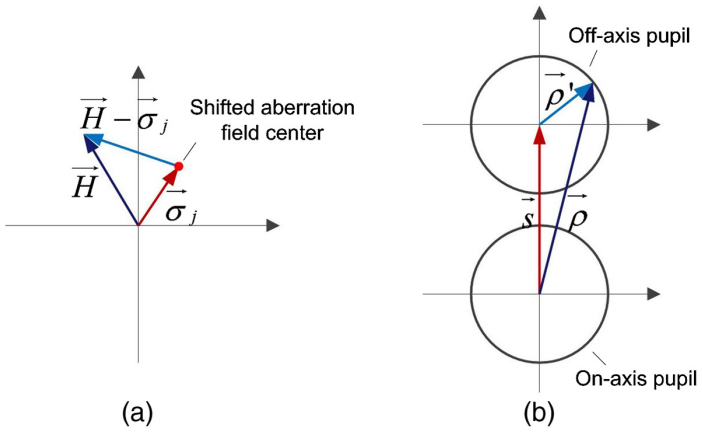

Fig. 2 Illustrations of (a) the shifted aberration field center for surface j and (b) the location of the off-axis pupil with reference to the on-axis pupil.

Here we first review the inherent relations between an astigmatism and a coma induced by lateral misalignments. In pupil-offset off-axis telescopes, the misalignment-induced aberrations can be decomposed into two parts, i.e., one part that is nearly the same as what exists in misaligned on-axis telescopes and another part that is generated from the aberrations (with a higher-order pupil dependence) of the misaligned on-axis system due to the effect of pupil offset. Here the "on-axis system" represents a conceptual rotationally symmetric system that has the same optical parameters with the off-axis system (e.g., thickness, radius of curvature, and conic) except the offset pupil. Specifically, when only the third-order aberrations of the on-axis system are considered, the analytic expressions for the net astigmatic and coma aberration contributions of lateral misalignments in off-axis system are presented in Eqs. (1) and (2),[13,16] respectively, i.e.,

$$W_{\mathrm{AST}} = (-\vec{A}_{222}\vec{H} - \vec{s}\vec{A}_{131}) \cdot \vec{\rho}^2, \tag{1}$$

$$W_{\mathrm{coma}} = -\vec{A}_{131} \cdot [\vec{\rho}(\vec{\rho} \cdot \vec{\rho})], \tag{2}$$

with

$$\vec{A}_{\mathrm{klm}} = \sum_j W_{\mathrm{klm}j}\vec{\sigma}_j. \tag{3}$$

In the above expressions, $\vec{H}$ is the normalized field vector, $\vec{\rho}$ is the normalized pupil vector, and $W_{\mathrm{klm}\,j}$ denotes the aberration coefficient for a particular aberration type of surface j. $\vec{\sigma}_j$ represents the position of the shifted aberration field center for this surface, which is linearly correlated with misalignments of the system.[22] $\vec{s}$ represents the location of the off-axis pupil with reference to the on-axis pupil, which is normalized by the radius of the pupil.

We can see that the misalignment-induced astigmatism contains two components, i.e., a field-linear component and field-constant component. The field-linear astigmatic component is nearly the same as what exists in misaligned on-axis systems. The field-constant astigmatism can be attributed to the effects of pupil offset, which converts the coma of the misaligned on-axis system to astigmatism of the misaligned off-axis system. The misalignment-induced coma only contains a field-constant component.

As discussed in reference,[13,16] the field-constant term in Eq. (1) is the dominant astigmatic component. In addition, in the global alignment process the bright star used for wavefront sensing will be adjusted to the central field position,[3] and we can consider $\vec{H} = \vec{0}$. Therefore, Eq. (1) can be rewritten as

$$W_{\mathrm{AST}} = -\vec{s}\vec{A}_{131} \cdot \vec{\rho}^2. \tag{4}$$

Comparing Eq. (2) with Eq. (4), we can recognize that in pupil-offset off-axis telescopes these two kinds of aberrations have some inherent relations. The inherent relations between the magnitude and orientation of astigmatism and coma can be roughly expressed as Eqs. (5) and (6), respectively, i.e.,

$$|\vec{C}_{\mathrm{AST}}| = 3|\vec{s}| \cdot |\vec{C}_{\mathrm{coma}}|, \tag{5}$$

$$2\phi_{\mathrm{AST}} = \phi_{\mathrm{coma}} + \theta_s, \tag{6}$$

where $|\vec{C}_{\mathrm{AST}}| \equiv \sqrt{(C_5)^2 + (C_6)^2}$, representing the magnitude of astigmatism and C_i is the i'th Fringe Zernike coefficient. $|\vec{C}_{\mathrm{coma}}| \equiv \sqrt{(C_7)^2 + (C_8)^2}$, representing the magnitude of coma. $|\vec{s}|$ is the magnitude of the pupil decenter vector. θ_s represents the azimuthal angle of the vector $\vec{s}$. ϕ_{AST} and ϕ_{coma} represent the orientation of astigmatism and coma, respectively. The underlying reason for this inherent relationship is that the field-constant astigmatism is mainly attributed to the effect of pupil offset, which converts the coma of the on-axis system to astigmatism of the off-axis system.

Although axial misalignments in the off-axis system can also introduce certain amount of astigmatism and coma,[14] for similar magnitudes of perturbations the astigmatism and coma induced by axial misalignments are usually far less than those induced by lateral misalignments. In fact, the inherent relationships between astigmatism and coma induced by lateral misalignments are also similar with those induced by axial misalignments.[14] In addition, we have also demonstrated that rotational misalignments can be converted to a special kind of lateral misalignments.[15]

Therefore, we can use Eqs. (5) and (6) to represent the inherent relations between the astigmatism and coma in pupil-offset off-axis systems in the presence of misalignments. Considering that each off-axis segment of the PM and the SMs compose an off-axis telescope in the global alignment process, Eqs. (5) and (6) will play an important role in the segment-level wavefront sensing approach proposed in this paper.

3 Segment-Level Wavefront Sensing Based on Analysis of PSF Image Features

In this section, we will propose an analytic approach of aberration estimation by analyzing geometric features of one defocused PSF. These geometric features include the lengths of the major axis and minor axis, and the azimuthal angle of the PSF at the image plane. One of the foundations of this approach is that when the magnitude of the wavefront aberration is comparatively large, the geometric shape of the PSF is mainly determined by the transverse aberrations of the marginal ray at the image plane, not the effect of diffraction. Meanwhile, the aberration properties of misaligned off-axis telescope also play an important role.

3.1 *Analytic Expression for the Elliptical Shape of the PSF Image*

For simplicity, we here first assume that the shape of each segment is circular. For each segment of the PM, the magnitude of $|\vec{s}|$ is equal to 2 or multiple of 2. Referring to Eq. (5), we can recognize that the magnitude of astigmatism is usually far larger than the magnitude of coma. Therefore, we can deduce that coma is not the dominant aberration that determines the shape of the PSF, and here we only consider defocus and astigmatism, which correspond to C_4 to C_6 Fringe Zernike aberration coefficients.

In this case, the segment-level wavefront phase can be approximated as

$$\Delta W(\rho,\phi) \approx C_4(2\rho^2-1) + C_5\rho^2\cos(2\phi) + C_6\sin(2\phi). \tag{7}$$

This expression can be rewritten as

$$\Delta W(\rho,\phi') \approx C_4(2\rho^2-1) + \sqrt{(C_5)^2+(C_6)^2}\cos(2\phi'), \tag{8}$$

where

$$\phi' = \phi - \theta_{\mathrm{AST}} \tag{9}$$

and

$$\cos(2\theta_{\mathrm{AST}}) = \frac{C_5}{\sqrt{(C_5)^2+(C_6)^2}}, \quad \sin(2\theta_{\mathrm{AST}}) = \frac{C_6}{\sqrt{(C_5)^2+(C_6)^2}}. \tag{10}$$

This operation can be seen as a rotational coordinate transformation, as shown in Fig. 3. Equation (8) can be expressed in Cartesian coordinates as

$$\Delta W(x',y') \approx 2C_4(x'^2+y'^2) + \sqrt{(C_5)^2+(C_6)^2}(x'^2-y'^2). \tag{11}$$

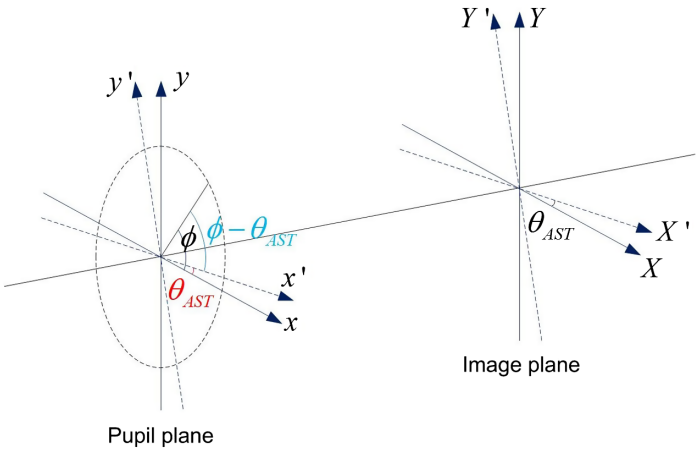

Fig. 3 Rotational coordinate transformation needed in the derivation.

The corresponding transverse aberrations of a ray in the two perpendicular directions can generally be expressed as[23]

$$\begin{aligned}\varepsilon_{X'} &= -\frac{R}{h}\frac{\partial \Delta W}{\partial x'},\\ \varepsilon_{Y'} &= -\frac{R}{h}\frac{\partial \Delta W}{\partial y'},\end{aligned} \tag{12}$$

where R is the radius of curvature of the nominal spherical wavefront, and h is geometrical pupil radius. By substituting Eq. (11) into Eq. (12), we can obtain that

$$\begin{aligned}\varepsilon_{X'} &= -4F^{\#}\left[2C_4x' + \sqrt{(C_5)^2+(C_6)^2}x'\right],\\ \varepsilon_{Y'} &= -4F^{\#}\left[2C_4y' - \sqrt{(C_5)^2+(C_6)^2}y'\right],\end{aligned} \tag{13}$$

where $F^{\#}$ represents the F number. Considering that the geometric figure of PSF is determined by the transverse aberrations of the marginal ray, we can only consider the case of $\rho = 1$. In other words, here we have

$$x'^2 + y'^2 = 1. \tag{14}$$

Combining Eqs. (13) and (14), we can finally obtain that

$$\begin{cases}\dfrac{(\varepsilon_{X'})^2}{\left\{4F^{\#}\left[2C_4+\sqrt{(C_5)^2+(C_6)^2}\right]\right\}^2} + \dfrac{(\varepsilon_{Y'})^2}{\left\{4F^{\#}\left[2C_4-\sqrt{(C_5)^2+(C_6)^2}\right]\right\}^2} = 1,\\ |2C_4| \neq \sqrt{(C_5)^2+(C_6)^2}.\end{cases} \tag{15}$$

This expression represents the geometric shape of the PSF, which is determined by the intersections of the marginal rays at the image plane. We can easily recognize that Eq. (15) represents an ellipse. In effect, this is an oblique ellipse in the standard coordinate system and the rotation angle is θ_{AST}. The physical meaning of $2|C_4| = \sqrt{(C_5)^2+(C_6)^2}$ is that the image plane is located at sagittal focal plane or meridional focal plane, in which case the elliptical PSF image degenerates into a line. The expressions of the lengths of major axis and minor axis depend on the sign of C_4. Specifically, if $C_4 > 0$, the length of the half major axis is $|4F^{\#}[2C_4 + \sqrt{(C_5)^2+(C_6)^2}]|$; otherwise, the length of the half major axis is $|4F^{\#}[2C_4 - \sqrt{(C_5)^2+(C_6)^2}]|$.

3.2 *Estimate of the Magnitudes and Orientations of the Wavefront Aberrations with a Defocused PSF Image*

The length of major axis $L_{\max}$ and the length of the minor axis $L_{\min}$ of the elliptical PSF can be expressed as

$$\begin{aligned}L_{\max} &= 8F^{\#}\left[|2C_4| + \sqrt{(C_5)^2+(C_6)^2}\right],\\ L_{\min} &= 8F^{\#}\left[\left||2C_4| - \sqrt{(C_5)^2+(C_6)^2}\right|\right].\end{aligned} \tag{16}$$

Therefore, we can obtain the magnitudes of the defocus aberration and astigmatism as

$$\begin{cases}\left\{\begin{array}{l}|C_4| = \frac{1}{32F^{\#}}(L_{\max}+L_{\min})\\ \sqrt{(C_5)^2+(C_6)^2} = \frac{1}{16F^{\#}}(L_{\max}-L_{\min})\end{array}\right\}, & \text{if } 2|C_4| \geq \sqrt{(C_5)^2+(C_6)^2},\\ \left\{\begin{array}{l}|C_4| = \frac{1}{32F^{\#}}(L_{\max}-L_{\min})\\ \sqrt{(C_5)^2+(C_6)^2} = \frac{1}{16F^{\#}}(L_{\max}+L_{\min})\end{array}\right\}, & \text{if } 2|C_4| < \sqrt{(C_5)^2+(C_6)^2}.\end{cases} \tag{17}$$

In practice, we can introduce a large positive defocus to realize $2C_4 > \sqrt{(C_5)^2 + (C_6)^2}$ by changing the axial position of the SM. (The SM is also axially translated in the focus sweep step.) Note that to satisfy the condition one needs to make assumptions about the magnitude of astigmatism based on tolerance. When the condition of $2C_4 > \sqrt{(C_5)^2 + (C_6)^2}$ is satisfied, we can see from Eq. (15) that the direction of the major axis of the PSF is in accordance with the direction of x' axis. Since the direction of x' axis is defined with reference to the direction of astigmatism (represented with θ_{AST}), we can deduce that in this case the direction of the major axis represents the direction of astigmatism, i.e.,

$$\theta_{\mathrm{AST}} = \theta_{\mathrm{MA}}, \tag{18}$$

where θ_{MA} represents the direction of the major axis of the elliptical PSF, as shown in Fig. 4. Then combining Eq. (10), Eqs. (17), and (18), we can obtain that

$$\begin{cases} C_5 = \frac{1}{16F^{\#}}(L_{\max} - L_{\min})\cos(2\theta_{\mathrm{MA}}), \\ C_6 = \frac{1}{16F^{\#}}(L_{\max} - L_{\min})\sin(2\theta_{\mathrm{MA}}). \end{cases} \tag{19}$$

The inherent relations between misalignment-induced astigmatism and coma shown in Eqs. (5) and (6) can be rewritten as

$$|\vec{C}_{\mathrm{coma}}| = |\vec{C}_{\mathrm{AST}}|/3|\vec{s}|, \tag{20}$$

$$\phi_{\mathrm{coma}} = 2\phi_{\mathrm{MA}} - \theta_s. \tag{21}$$

Therefore, we can further obtain the coma aberration coefficients as

$$\begin{cases} C_7 = \sqrt{(C_5)^2 + (C_6)^2}\cos(2\theta_{\mathrm{MA}} - \theta_s)/3|\vec{s}|, \\ C_8 = \sqrt{(C_5)^2 + (C_6)^2}\sin(2\theta_{\mathrm{MA}} - \theta_s)/3|\vec{s}|. \end{cases} \tag{22}$$

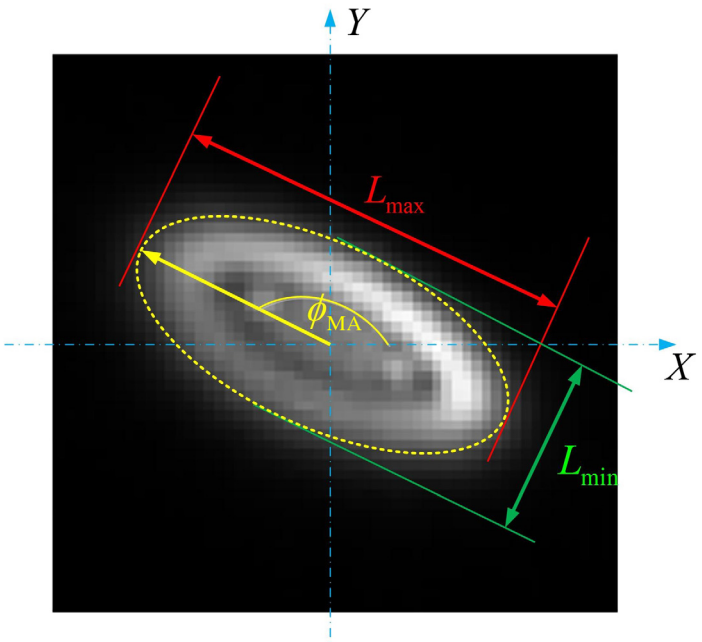

Fig. 4 Illustration of the major axis length $L_{\max}$, minor axis length $L_{\min}$, and azimuth angle θ_{MA} of the PSF.

3.3 *Other Discussions*

In this section, we derive the analytic relationships between the geometric figures of the PSF and the dominant wavefront aberrations. On this basis, we can determine these dominant aberrations with only one defocused PSF image.

Here we continue to present some other in-depth discussions for a better understand of this analytic wavefront sensing approach, which are shown as follows.

(1) When the imaging plane is located at the sagittal focal plane or meridional focal plane the relationship between defocus and astigmatism is $2|C_4| = \sqrt{(C_5)^2 + (C_6)^2}$. In these two cases, the PSF degenerates into a line. For a certain optical system, the length of this line is mainly determined by astigmatism, which is about $16F^{\#}\sqrt{(C_5)^2 + (C_6)^2}$. The positions of sagittal focal plane or meridional focal plane will change if the magnitude of astigmatism changes.

(2) In the process of introducing a positive defocus aberration to the system, the trend of the change in PSF shape is dependent on the current position of the image plane. When the image plane is located between the sagittal and meridional focal plane, i.e., $2|C_4| < \sqrt{(C_5)^2 + (C_6)^2}$, the sum of the lengths of the major axis and minor axis of the PSF will stay unchanged if we introduce a positive defocus to the system. Otherwise, the major axis length and minor axis length will increase or decrease at the same time, if we introduce a positive defocus aberration. We can use this knowledge to determine if the condition of $2C_4 > \sqrt{(C_5)^2 + (C_6)^2}$ is satisfied when we introduce a positive defocus aberration to the system.

(3) The sign of the defocus aberration determines whether the direction of astigmatism is in accordance with the direction of the major axis of the PSF. Specifically, if $C_4 > 0$, the direction of astigmatism is in accordance with the direction of the major axis of the PSF; if $C_4 < 0$, the direction of astigmatism is perpendicular to the direction of the major axis of the PSF.

(4) Mathematically speaking, if the signs of the defocus aberration and astigmatism change at the same time, the shape of the PSF will stay unchanged. However, the relationships between astigmatism and coma for a certain off-axis system can serve as a tool to eliminate the ambiguity inherent in phase retrieval with only one PSF image. (The direction of coma is roughly in accordance with the direction of the center-of-gravity shift of the PSF.) Specifically, we can first estimate the direction of coma according to the direction of the center-of-gravity shift of the PSF; then we can obtain the direction astigmatism according to the relationship between misalignment-induced astigmatism and coma; finally, we can further determine the sign of defocus by comparing the direction of astigmatism with the direction of the major axis of the PSF. Therefore, although in the paper we eliminate this ambiguity by introducing a large positive defocus to realize the condition of $2C_4 > \sqrt{(C_5)^2 + (C_6)^2}$, it is possible that we can handle this problem without any other auxiliary operation.

4 Simulations

4.1 *Optical System and Simulation Procedure*

In this section, the optical system of the JWST will be used to demonstrate the effectiveness of the proposed approach through simulation. The optical layout of the JWST is shown in Fig. 5, and the optical parameters of this telescope are shown in Table 1.[1] The PM of JWST is composed of 18 hexagonal segments and the aperture size each segment is 1.3 m. Note that the tertiary mirror (TM) and the fine steering mirror (FSM) are decentered in the y direction in the nominal state.

In the simulation, the TM is set as the coordinate basis, and the misalignments of the PM and SM are defined with reference to TM. The simulation procedures are summarized as follows.

(1) One set of misalignments of each PM segment and SM is randomly generated within certain perturbation range and introduced to the optical simulation software Zemax.

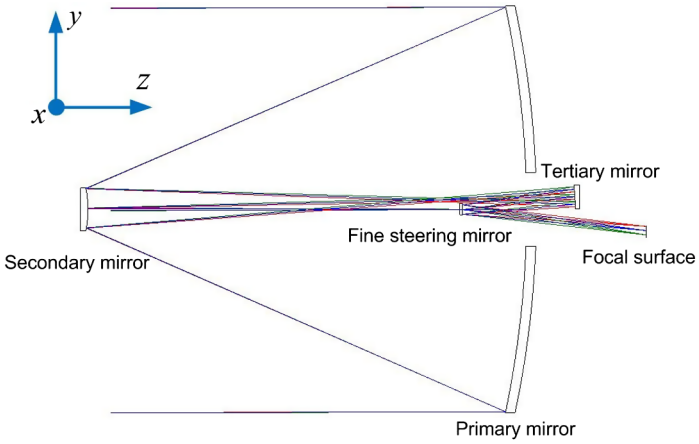

Fig. 5 Optical layout of the JWST.

Table 1 Specifications of the JWST.

Surface	Radius (mm)	Conic	Thickness (mm)	Decenter_Y (mm)
PM	−15879.7	−0.9967	−7169.0	0
SM	−1778.9	−1.6598	7965.3	0
TM	−3016.2	−0.6595	−1844.1	−0.19
FSM	∞	—	2999.0	−2.36

Table 2 Misalignment ranges for PM segments and SM.

XDE (mm)	YDE (mm)	ZDE (mm)	ADE (deg)	BDE (deg)
[−0.5,0.5]	[−0.5,0.5]	[−0.3,0.3]	[−0.01,0.01]	[−0.01,0.01]

The perturbation ranges of PM segments and SM are shown in Table 2. Here we suppose that the misalignment range in the axial direction (ZDE) is smaller than those in the lateral direction (XDE and YDE) since in the SM focal sweep process (this process is prior to global alignment, as shown in Fig. 1) the axial misalignments can be partly corrected.

(2) For each subsystem composed by each PM segment and the SMs, on one hand, the aberration coefficients of it are saved and they will serve as the standard values; on the other hand, the PSF image of each subsystem is obtained from the optical simulation software. Meanwhile, a positive defocus aberration (about $+1.5\lambda$ and $1\lambda = 1\ \mu$m) is introduced to the system by axially shifting the SM (by 0.8 mm) in advance to guarantee $2C_4 > \sqrt{(C_5)^2 + (C_6)^2}$.

(3) After some proper pretreatments (such as smoothing filtering), threshold segmentation operation is performed to determine the effective region of the elliptical PSF. Then the lengths of major and minor axis as well as the azimuth angle of the major axis are calculated using MATLAB®.

(4) The aberration coefficients of each subsystem are estimated using the proposed approach. Note that different subsystems have different normalized aperture offset vectors, which determine the inherent relations between astigmatism and coma in the misalignment state.

(5) The accuracy of the proposed approach is evaluated by comparing the aberration coefficients obtained from the simulation software to those analytically calculated.

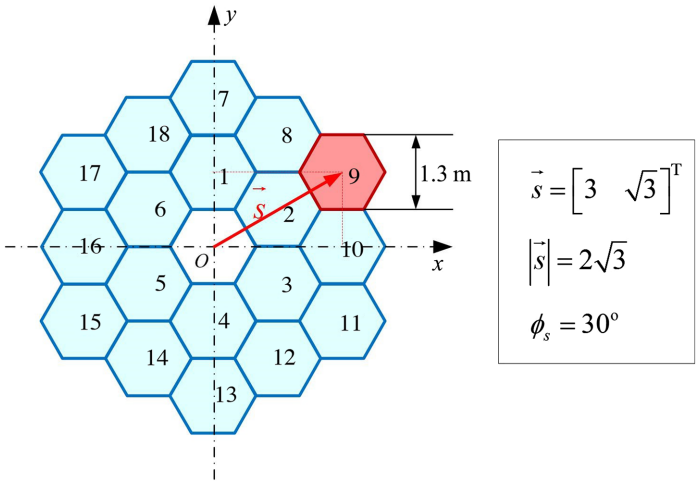

Fig. 6 The position of the segment considered in this simulation.

4.2 *Illustration of the Specific Application Procedures for One Subsystem*

We here first illustrate the application procedures of the proposed approach for one subsystem composed by one PM segment and the SMs. The considered PM segment is shown in Fig. 6 (in red color), which also presents the specific value of the corresponding vector $\vec{s}$. (When the shape of the segments is not circular, the magnitude of $|\vec{s}|$ is no longer 2 or a multiple of 2.) This vector is used to estimate the magnitude and direction of coma using the magnitude and direction of astigmatism. The superscript T represents transposition operation. The specific misalignments of the PM segment and the SM are shown in Table 3.

The PSF image obtained from the optical simulation software (after introducing a positive defocus aberration) and the binary image after threshold segmentation are shown in Figs. 7(a) and 7(b), respectively. Meanwhile, we suppose the pixel size is 20 μm. The field position is (0 deg, 0 deg). (The aberrations in the nominal state in this field can be neglected for a subsystem.) The threshold value for segmentation is selected as 5% of the peak value of the PSF.

Table 3 Specific misalignment parameters for SM and the PM segments shown in Fig. 6.

	XDE (mm)	YDE (mm)	ZDE (mm)	ADE (deg)	BDE (deg)
PM segment	−0.20	0.30	−0.15	−0.002	0.003
SM	−0.30	−0.40	0.01	−0.003	−0.005

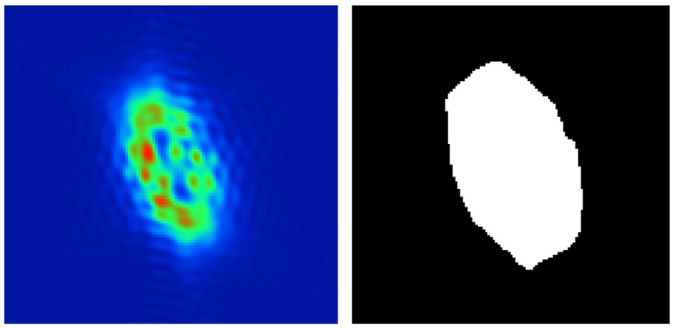

(a) (b)

Fig. 7 (a) PSF image obtained from the simulation software and (b) the binary image after threshold segmentation, which is used to determine the effective region of the PSF.

Table 4 The aberrations obtained from the simulation software and those analytically calculated.

	C_4	C_5	C_6	C_7	C_8	Mean error
Standard	0.910	−0.404	−0.364	−0.059	−0.017	0.0218
Calculated	0.921	−0.366	−0.324	−0.046	−0.010	

These aberration coefficients are in λ ($\lambda = 632.8$ nm).

The aberration coefficients obtained from the optical simulation software and those analytically calculated are shown in Table 4. We can see that the mean error is about 0.022 waves, which indicates a high estimation accuracy.

Some other discussions concerning the above simulation are presented as follows.

(1) The accuracy of the calculated aberration coefficients is related with the threshold value for determining the effective region of PSF. (In the above simulation, this value is 5% of the peak value of the PSF image.) If the ratio of the peak value for threshold segmentation is changed, the accuracy will change accordingly, as shown in Fig. 8. However, we can also find that while the accuracy of the calculated defocus aberration is very sensitive to the variation in this value, the accuracies of the astigmatism (C_5, C_6) and coma (C_7, C_8) are not sensitive to the variation in this value. Considering that these nonrotationally symmetric aberrations are more important for alignment, this method is robust to the variation in the threshold value for segmentation.

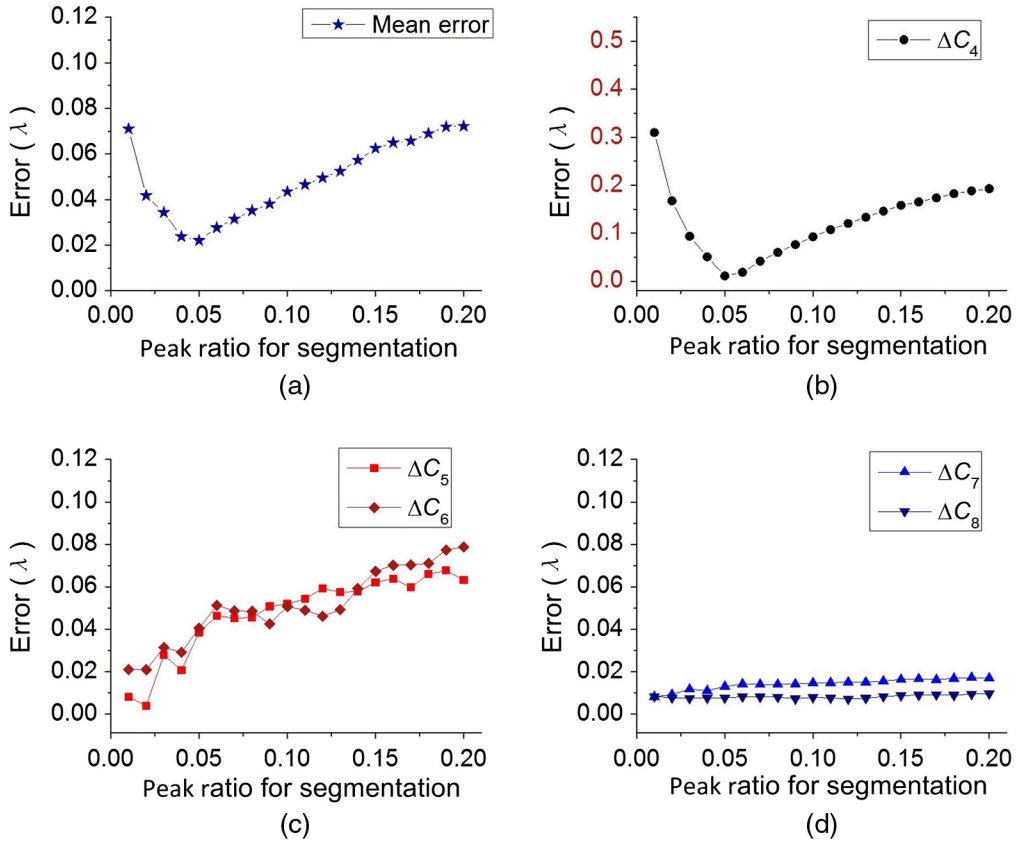

Fig. 8 Variations in the accuracies of the analytically calculated aberration coefficients due to the variation in the threshold value for segmentation. Here the threshold value is evaluated according to the ratio of the peak value of the PSF. (a) The variation in the mean error of the five dominant aberration coefficients (C_4 to C_8). (b)–(d) The variations in the accuracies of defocus (C_4), astigmatism (C_5, C_6), and coma (C_7, C_8), respectively. We can see that the accuracies in astigmatism and coma are not sensitive to the variation in threshold value.

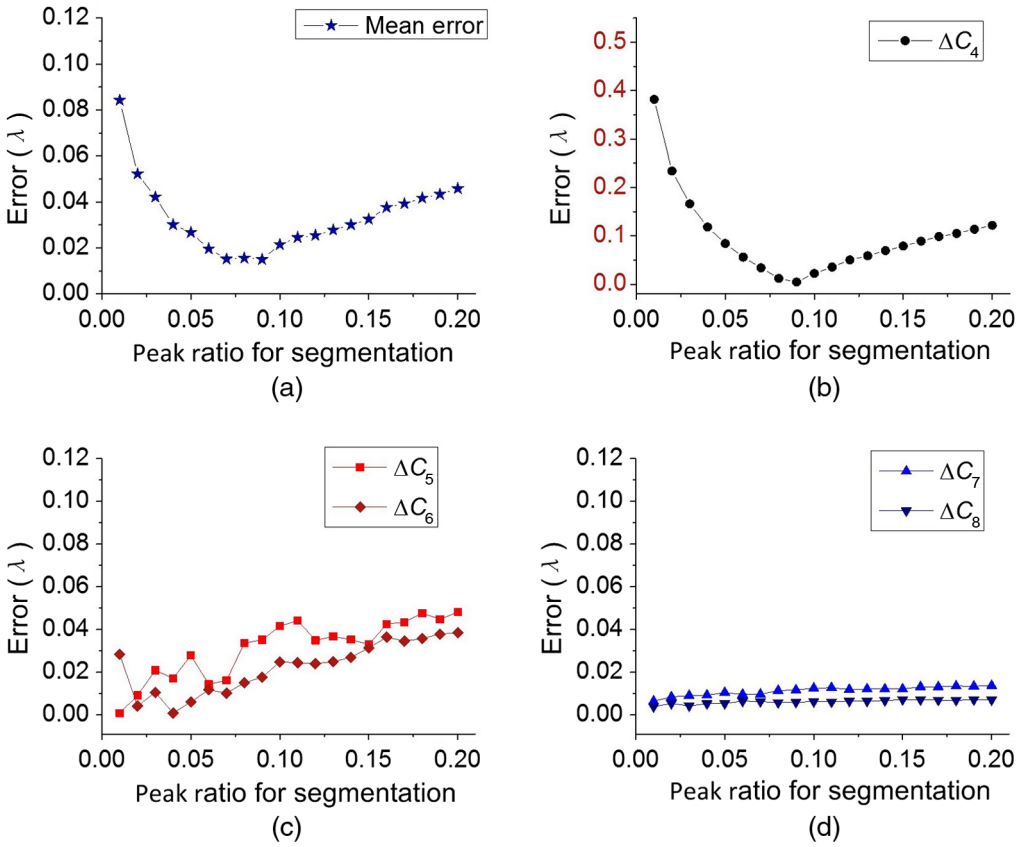

Fig. 9 The accuracies of the analytically calculated aberration coefficients for a circular aperture. (a) The variation in the mean error of the five dominant aberration coefficients (C_4 to C_8). (b)–(d) The variations in the accuracies of defocus (C_4), astigmatism (C_5, C_6), and coma (C_7, C_8), respectively. Comparing this figure with Fig. 8, where a hexagonal aperture is used, we can recognize that the shape of aperture does not impose a large influence on the accuracies of the calculated aberration coefficients.

(2) While in Sec. 3 we consider a circular pupil, in the above simulation, the shape of the segment is hexagonal. This can introduce some error in aberration estimation. In the presence of a circular segment, the accuracies of the analytically calculated aberration coefficients that vary with threshold value for segmentation are shown in Fig. 9. We can see from Fig. 9(a) that the least value of the mean error is about 0.01 waves. The accuracy of the calculated astigmatism is also a little higher than that shown in Fig. 8. However, we can still recognize that the deviation between Figs. 8 and 9 is not obvious. In other words, the analytic approach proposed in Sec. 3 is well applicable to hexagonal apertures.

(3) The reason for why the accuracies of the recovered astigmatic aberration coefficients are robust to the threshold value is that astigmatic aberration coefficients are determined by the difference between the length of the major axis and the length of the minor axis when the condition of $2C_4 > \sqrt{(C_5)^2 + (C_6)^2}$ is satisfied, as shown in Eq. (17). Although the actual major axis length and minor axis length are sensitive to the threshold value for segmentation, the variation in the difference of them is very small. Defocus aberration is linearly related with the sum of the lengths of the major axis and the minor axis. Therefore, the calculated defocus aberration is more sensitive to the selection of threshold value. However, in practice, we can still select a suitable threshold value for the estimation of the defocus aberration by trial and error.

4.3 *Simulation Results for the Whole 18 Subsystems*

After illustrating the specific procedures for an individual segment-level wavefront sensing process, we continue to perform segment-level wavefront sensing for the whole 18 subsystems.

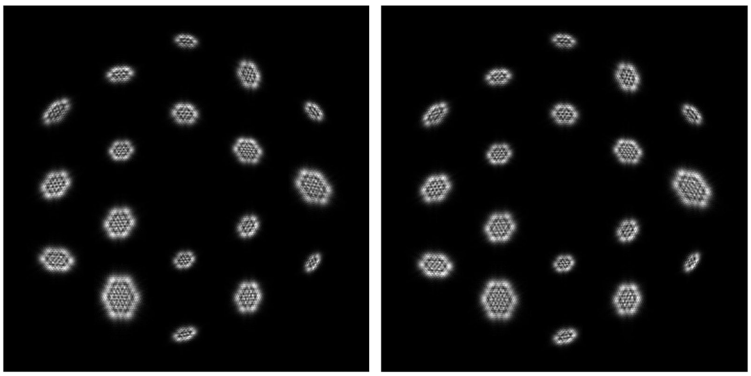

Fig. 10 (a) The PSFs corresponding to the 18 subsystems directly obtained from the optical simulation software and (b) those reconstructed using the recovered aberration coefficients according to Fourier optics. We can recognize a significant similarity between these two sets of PSFs, which indicates a high estimate accuracy of the recovered aberration coefficients.

A set of misalignment parameters (including misalignments of each PM segment and the SM) is randomly generated within the perturbation ranges shown in Table 2. The PSFs corresponding to the 18 subsystems obtained from the optical simulation software are shown in Fig. 10(a). For each PSF, we can obtain a set of aberration coefficients with the proposed approach. Meanwhile, the segmentation ratio is the same as that used for Table 4. (The threshold is 5% of the peak value of PSF.) For each set of the recovered aberration coefficients, we can reconstruct one PSF image according to Fourier optics, which are shown in Fig. 10(b). We can see that these two sets of PSFs are very similar, and we can hardly recognize the differences between them unless we expand the sizes of the PSFs and examine them carefully. This fact indicates that the proposed approach has a high aberration estimation accuracy.

Finally, Monto Carlo simulations are further performed to demonstrate the accuracy of the proposed approach. Specifically, 100 sets of misalignment parameters of the PM segments and the SM are randomly generated within the misalignment ranges shown in Table 2. For each set of misalignment parameters, we can obtain 18 defocused PSFs. (A positive defocus aberration is introduced to the system by changing the axial position of the SM by 0.8 mm in advance.) Then using the approach proposed in this paper, we can obtain 18 sets of aberration coefficients. Comparing these aberration coefficients with those obtained from the optical simulation software, we can obtain the absolute error of each aberration coefficient for each segment. The mean errors of different aberration coefficients (C_4 to C_8) for 100 sets of misalignment states are shown in Table 5. The mean values of each aberration coefficient for the whole 18 segments are also presented in Table 5, which can represent the estimation accuracy for each aberration coefficient. We can recognize that the estimation accuracy for defocus aberration is comparatively low, which is partly determined by the segmentation ratio. The estimation accuracy for coma aberration is high, partly because the magnitude of coma aberration is originally small. In addition, we can also recognize that the estimation accuracy for 0 deg and 45 deg astigmatism is different. The underlying reason is that the hexagonal shape of each segment loses rotational symmetry. The calculation of the major axis and minor axis of the PSF may be more accurate in 45 deg direction, which leads to a relatively high estimation accuracy for 45 deg astigmatism.

5 Experiment

In this section, we will further perform an experiment to demonstrate the effectiveness of the proposed approach. The sketch and physical map of the experimental setup are shown in Figs. 11(a) and 11(b), respectively. The optical system in this experimental setup is composed by only one lens. The aberrations of the system are introduced by tip-tilting the lens (so that an off-axis field is used) and transversely translating the aperture stop (so that an off-axis aperture is used).

Table 5 The results of Monte Carlo simulations for each segment.

Segment index	$\overline{\lvert\Delta C_4\rvert}$	$\overline{\lvert\Delta C_5\rvert}$	$\overline{\lvert\Delta C_6\rvert}$	$\overline{\lvert\Delta C_7\rvert}$	$\overline{\lvert\Delta C_8\rvert}$
1	0.0447	0.0241	0.0140	0.0025	0.0108
2	0.0423	0.0221	0.0136	0.0092	0.0053
3	0.0403	0.0219	0.0150	0.0078	0.0060
4	0.0407	0.0230	0.0156	0.0028	0.0112
5	0.0430	0.0209	0.0140	0.0081	0.0057
6	0.0433	0.0228	0.0150	0.0083	0.0065
7	0.0367	0.0421	0.0278	0.0020	0.0186
8	0.0418	0.0396	0.0351	0.0096	0.0164
9	0.0399	0.0427	0.0291	0.0163	0.0088
10	0.0382	0.0445	0.0269	0.0189	0.0020
11	0.0487	0.0436	0.0306	0.0168	0.0093
12	0.0390	0.0412	0.0322	0.0084	0.0165
13	0.0437	0.0397	0.0298	0.0022	0.0193
14	0.0365	0.0443	0.0332	0.0086	0.0162
15	0.0377	0.0357	0.0300	0.0158	0.0093
16	0.0366	0.0454	0.0243	0.0190	0.0018
17	0.0380	0.0370	0.0268	0.0158	0.0091
18	0.0395	0.0368	0.0381	0.0096	0.0160
Mean	0.0406	0.0348	0.0250	0.0100	0.0105

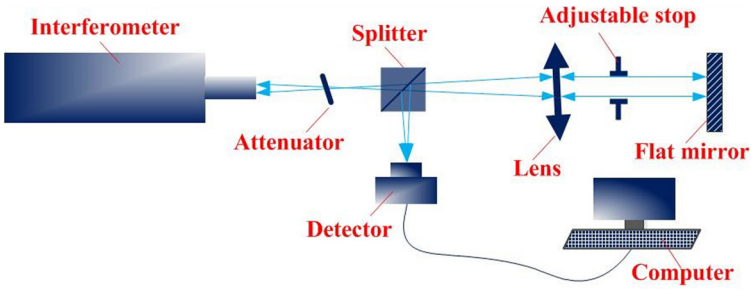

(a)

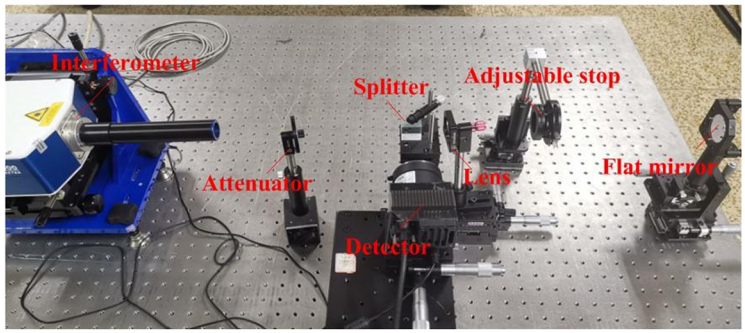

(b)

Fig. 11 (a) The sketch and (b) physical map of the experimental setup.

The interferometer (PhaseCam 6000) in Fig. 11 plays two major roles. On one hand, it can directly measure the aberrations of the optical system in certain aberrational state. The results of interferometer will be compared to results of the proposed approach to demonstrate the accuracy of the proposed approach. On the other hand, the focus of interferometer is used to serve as a point light source that coincides with the focus of the lens. The beam passes through the system two times and a PSF can be obtained with the detector. The detector is placed on an adjustable translation stage, and therefore, the position of detector can be controlled (i.e., we can obtain positively defocused PSFs by adjusting the axial position of detector). The focal length of the lens is 180 mm, the wave length is 0.6328 μm, and the pixel size of the detector is 5.5 μm.

The experimental procedures are shown as follows.

(1) Adjust the pose of the lens and the size and positon of the aperture stop.
(2) Measure the aberrations of the optical system using the interferometer, and the results will serve as the standard value to demonstrate the accuracy of the proposed approach.
(3) Adjust the axial position of the detector and collect several positively defocused PSFs with the detector.
(4) Apply the proposed approach to the collected defocused PSFs. The average value of the results will be compared to those directly measured by the interferometer.

Note that in this experiment we mainly validate the accuracy of the astigmatic aberration coefficients. The reasons are presented below. On one hand, we cannot demonstrate the estimation accuracy of the defocus aberration since the detector of the interferometer and the detector used to collect PSF images are generally located at different axial positions. On the other hand, as presented before, the magnitude of coma is comparatively small and we here neglect them; in addition, for the optical system composed by only one lens with a large field of view, the relationship between astigmatism and coma presented in Eqs. (5) and (6) is no longer valid (i.e., in this case, we cannot estimate coma from astigmatism).

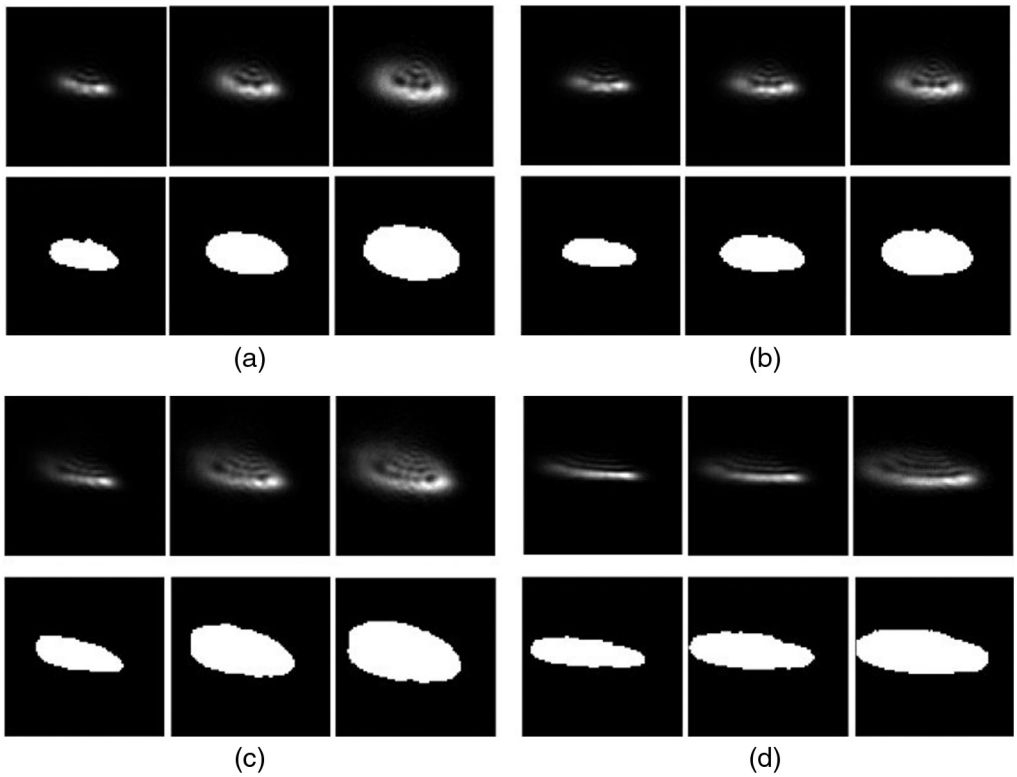

Fig. 12 (a)–(d) Four sets of PSF images (including the binary images after segmentation) corresponding to four aberrational states. In each of them, there are three PSF images, which correspond to one aberrational state but are obtained at different axial positions (different focal planes).

We repeat the experimental procedures for four times, i.e., we measure four sets of aberration coefficients and collect four sets of PSF images. Each set includes three PSF images, which are all positively defocused but with different magnitudes of defocus aberration. The four sets of PSFs as well as the corresponding binary images are shown in Fig. 12.

The four sets of aberration coefficients (C_5 to C_9) corresponding to the four aberrational states that are measured with interferometer are presented in Table 6. The aperture size for these four sets of data is 6.1, 7.3, 8.2, and 8.5 mm, respectively. The reason for us to change the aperture size is to maintain the ratio between the magnitude of astigmatism and coma aberration. We can see from Table 6 that the ratios between the magnitude of astigmatism and coma aberration for the four sets of aberrations are all close to 5. Here we want to make the experiment be in accordance to the cases where $|\vec{s}| = \sqrt{3}$ and $3|\vec{s}| \approx 5$.

Then we apply the analytic approach to these positively defocused PSFs and obtain one set of astigmatic aberration coefficients for each PSF. The average of the three sets of aberration coefficients correspond to one aberrational state will be taken as the result of the proposed approach. Then these calculated coefficients are compared to those measured by interferometer. The results are presented in Table 7.

We can see that the proposed approach can calculate the dominant aberrations with one defocused PSF. The mean absolute error between the coefficients calculated with the proposed approach and those measured with the interferometer is about 0.035λ. On one hand, we can see from Table 7 that the magnitudes of the calculated coefficients are all smaller than those measured. This fact indicates that there exists some systematic error and one of the possible sources is the nonpath error due to the presence of splitter. On the other hand, we also point out that in this experiment the shape of the aperture stop is near circular (different from the case in simulation where hexagonal aperture is used), which will improve the accuracy of the

Table 6 The four sets of aberration coefficients measured with interferometer.

Index	C_5	C_6	C_7	C_8	C_9
1	0.449	−0.201	0.061	−0.096	0.028
2	0.581	−0.142	0.077	−0.103	0.026
3	0.717	−0.407	0.132	−0.160	0.039
4	1.198	−0.306	0.145	−0.196	0.037

These aberration coefficients are in λ ($\lambda = 632.8$ nm).

Table 7 Comparisons between astigmatic aberration coefficients measured with interferometer and those analytically calculated.

Index	Method	C_5	C_6
1	Interferometer	0.449	−0.201
	Analytic approach	0.410	−0.174
2	Interferometer	0.581	−0.142
	Analytic approach	0.568	−0.113
3	Interferometer	0.717	−0.407
	Analytic approach	0.690	−0.365
4	Interferometer	1.198	−0.306
	Analytic approach	1.146	−0.254

These aberration coefficients are in λ ($\lambda = 632.8$ nm).

recovered aberration coefficients to some extent. In addition, we can also recognize that the presence of other aberrations (such as coma) does not impose a large influence on the calculation of astigmatic aberration coefficients.

6 Conclusion

In this paper, an analytic approach is proposed to estimate the segment-level wavefront aberrations of segmented mirror space telescopes in the global alignment process. In this approach, the relationships between the wavefront aberration coefficients and the geometric features of one defocused PSF are established. These geometric features include the lengths of the major axis and minor axis, and the azimuthal angle of the PSF at the image plane. One of the foundations of this approach is that when the magnitude of the wavefront aberration is comparatively large, the shape of the PSF is mainly determined by the geometric transverse aberrations of the marginal ray at the image plane, not the effects of diffraction. Therefore, we can accurately estimate the wavefront aberration coefficients with geometric features of the defocused PSF.

Another foundation of this approach is the special aberration property of misaligned off-axis system. Segment-level wavefront sensing before image stacking can be seen as wavefront sensing for a series of off-axis subsystems. (Each off-axis subsystem has a unique aperture offset.) The aberration property of misaligned off-axis telescopes plays two important roles in this analytic approach. On one hand, coma is not the dominant aberrations in misaligned off-axis systems compared to astigmatism and defocus, and therefore, we can only consider astigmatism and defocus when formulating the geometrical shape of the PSF; on the other hand, coma has quantitative relations with astigmatism when the system is in the misaligned state, and therefore, we can estimate coma aberration coefficients from the values of the astigmatism aberration coefficients.

Note that there exists an ambiguity between the PSF features and the corresponding wavefront aberration coefficients, as shown in Eq. (17). We eliminate this ambiguity by artificially introducing a large positive defocus aberration. (For JWST, we can easily achieve this goal by axially translating the position of the SM.) In this case, the relations between wavefront aberration coefficients and the PSF geometric features are simple and deterministic.

This approach can not only be applicable to segment-level wavefront sensing in global alignment for segmented mirror space telescopes, but also can directly be applied to wavefront sensing of monolithic mirror off-axis telescopes. Meanwhile, some insights are also provided into the relations between the geometric features of PSF and the wavefront aberrations.

Acknowledgments

This research was supported by the National Key Research and Development Program (No. 2016YFE0205000) and the National Natural Science Foundation of China (NSFC) (Nos. 61905241, 61705223, and 61805235).

References

1. P. A. Lightsey et al., "James Webb Space Telescope: large deployable cryogenic telescope in space," *Opt. Eng.* **51**(1), 011003 (2012).
2. M. Clampin, "Status of the James Webb Space Telescope Observatory," *Proc. SPIE* **8442**, 84422A (2012).
3. L. D. Feinberg et al., "TRL-6 for JWST wavefront sensing and control," *Proc. SPIE* **6687**, 668708 (2007).
4. D. Scott Acton et al., "Demonstration of the James Webb Space Telescope commissioning on the JWST testbed telescope," *Proc. SPIE* **6265**, 62650R (2006).
5. D. Scott Acton et al., "Wavefront sensing and controls for the James Webb Space Telescope," *Proc. SPIE* **8442**, 84422H (2012).
6. M. D. Perrin et al., "Preparing for JWST wavefront sensing and control operations," *Proc. SPIE* **9904**, 99040F (2016).

7. J. E. Krist and C. J. Burrows, "Phase-retrieval analysis of pre-and post-repair Hubble Space Telescope images," *Appl. Opt.* **34**, 4951–4964 (1995).
8. J. R. Fienup et al., "Hubble space telescope characterized by using phase retrieval algorithms," *Appl. Opt.* **32**, 1747–1767 (1993).
9. R. W. Gerchberg and W. O. Saxton, "A practical algorithm for the determination on phase from image and diffraction plane pictues," *Optik* **35**, 237–250 (1972).
10. D. L. Misell, "An examination of an iterative method for the solution of the phase problem in optics and electron optics," *J. Phys. D* **6**, 2200–2216 (1973).
11. R. A. Gonsalves, "Phase retrieval and diversity in adaptive optics," *Opt. Eng.* **21**, 829–832 (1982).
12. R. G. Paxman, T. J. Schulz, and J. R. Fienup, "Joint estimation of object and aberrations by using phase diversity," *J. Opt. Soc. Am. A* **9**(7), 1072–1085 (1992).
13. G. Ju et al., "Aberration fields of off-axis two-mirror astronomical telescopes induced by lateral misalignments," *Opt. Express* **24**(21), 24665–24703 (2016).
14. G. Ju et al., "Nonrotationally symmetric aberrations of off-axis two-mirror telescopes induced by axial misalignments," *Appl. Opt.* **17**(6), 24665–24703 (2018).
15. G. Ju, H. Ma, and C. Yan, "Aberration fields of off-axis astronomical telescopes induced by rotational misalignments," *Opt. Express* **26**(19), 24816–24834 (2018).
16. G. Ju et al., "Experimental study on the extension of nodal aberration theory to pupil-offset off-axis three-mirror anastigmatic telescopes," *J. Astron. Telesc. Instrum. Syst.* **5**(2), 029001 (2019).
17. R. A. Buchroeder, "Tilted component optical systems," PhD Dissertation, University of Arizona, Tucson, Arizona (1976).
18. R. V. Shack and K. P. Thompson, "Influence of alignment errors of a telescope system on its aberration field," *Proc. SPIE* **0251**, 146–153 (1980).
19. K. Thompson, "Description of the third-order optical aberrations of near-circular pupil optical systems without symmetry," *J. Opt. Soc. Am. A* **22**(7), 1389–1401 (2005).
20. T. Schmid, K. P. Thompson, and J. P. Rolland, "Misalignment-induced nodal aberration fields in two-mirror astronomical telescopes," *Appl. Opt.* **49**(16), D131–D144 (2010).
21. K. P. Thompson, T. Schmid, and J. P. Rolland, "The misalignment induced aberrations of TMA telescopes," *Opt. Express* **16**(25), 20345–20353 (2008).
22. K. P. Thompson et al., "Real-ray-based method for locating individual surface aberration field centers in imaging optical systems without rotational symmetry," *J. Opt. Soc. Am. A* **26**(6), 1503–1517 (2009).
23. D. Malacara, *Optical Shop Testing*, John Wiley & Sons, New Jersey (2007).

Guohao Ju is a researcher at Changchun Institute of Optics, Fine Mechanics and Physics, Chinese Academy of Science. His major interest is in both aberration theory and image-based wavefront sensing methods.

Boqian Xu is a professor at CIOMP who specializes in the fabrication of space-based large-aperture segmented telescopes.

Di Zhang is currently studying for an image processing doctoral degree at CIOMP, majoring in machine learning.

Hongcai Ma is a professor at CIOMP who specializes in active optics and optical simulations.

Xiaoquan Bai is a student at CIOMP, majoring in aberration theories.